VISCOELASTIC RESPONSE OF THE THORAX UNDER DYNAMIC LOADING

Asst. Prof. Dr. Mohsin Noori Hamzah
Machines & Equipment Engineering Department
University of Technology, IRAQ
dr.mohsin@uotechnology.edu.iq

ABSTRACT

In this paper, the contribution and constitutive modelling of the intercostal muscles (ICM) in a computational thorax FE model is studied. This helps in improving our knowledge to predict the number and locations of the fractured ribs during automotive accidents. ICM demonstrates a number of complex features including nonlinearity, viscoelasticity, and anisotropy. These muscles consist of an external and an internal layer, each of them having its own fiber orientation.

Tensile tests were performed on ICM samples harvested from one cadaver. Each specimen consisted of a 15 mm-long rectangle of ICM connected to the adjacent superior and inferior sections of the ribs. The load and applied displacement were measured. An optical system (ARAMIS) was used to measure the strain field on the external layer. Preconditioning, ramp and hold (relaxation), and quasi-static failure tests were performed.

The hyperelastic material parameters were estimated through an optimization process based on the experimental force–displacement curves of the quasi-static tensile tests. The results of the parameters optimization revealed that the ICM exhibited a high degree of anisotropy. The identification of the viscoelastic parameters was accomplished from the ramp and hold (relaxation) tests using Prony series.

استجابة الصدر المرنة ـ اللزجة تحت تأثير الاحمال الديناميكية

الخلاصة

تم في هذا البحث دراسة مساهمة ونمذجة العضلات الوربية في النموذج الحسابي الرقمي للصدر باستخدام العناصر المحددة. وهذا يساعد في تحسين معرفتنا للتنبؤ بعدد ومواقع الأضلاع المكسورة أثناء حوادث السيارات. تملك العضلات الوربية خصائص معقدة، حيث ان تصرفها لا خطي، لزجة، وتتباين خصائصها مع تغير الاتجاه. تتألف هذه العضلات من طبقة خارجي واخرى داخلية، ولكل منها اتجاه الياف خاصة به.

أجريت الاختبارات على عينات شد لعضلات وربية بشرية. وتألفت كل عينة من مستطيل بطول 15مم من العضلات الوربية متصلة مع الأضلاع العليا والدنيا (المقطوعة) المجاورة. تم قياس الحمل والاستطالات الناتجة اثناء الاختبار. كما تم استخدام نظام بصري (أراميس) لقياس توزيع الانفعال على الطبقة الخارجية. أجريت اختبارات التهيئة المسبقة، اختبارات الاسترخاء، واختبارات الفشل شبه-الثابت على جميع العينات.

خمنت معلمات المواد المفرطة-المرونة من خلال عملية الحل الامثل اعتمادا على منحنيات القوة-الازاحة لاختبارات الشد شبه-الثابت. أظهرت النتائج بان العضلات الوربية تملك درجة عالية من التباين في الخواص. اما المعلمات الخاصة بالتصرف اللزج للمادة فقد تم حسابها على أساس اختبارات الاسترخاء باستخدام سلسلة بروني.

1. INTRODUCTION

The increase in road traffic accidents contribute to higher rates of injuries resulting from seat belt use. Chest and/or abdominal abrasion at the site of seat belt contact are commonly seen, and with the exception of subcutaneous bruising, the sternal and ribs fracture is the most common seat belt injury. Therefore, the prediction of rib fractures using a computational thorax model remains an important and elusive challenge, as the finite element (FE) currently models generally fail to match both the number and the location of the fractures reported during experimental tests. Although a large body of research dealing with the thorax injury tolerance, the available thorax FE models are still missing to include the contribution of the intercostal muscles (ICM). Several models have been developed to model the response of the chest or the entire body under a variety of loading conditions [1]-[6], based on the work performed to determine the material properties of various isolated thoracic components, including clavicles [7], ribs [8]-[9] and costal cartilage [10]-[11]. The contribution of the intercostal muscles, in modelling the thorax, received, relatively, little attention [12], besides, very little work on the constitutive modeling of intercostal muscles [12].

Finite element modeling facilitates the simulation of thoracic impacts using a wide variety of boundary conditions, material properties and other variables than would not be possible to evaluate experimentally due to cost, material availability, instrumentation limitations or physical constraints. FE modeling of the thorax helps to improve the understanding of the injury mechanisms in the ribs, and consequently more accurate FE models that account for the contribution of each anatomical component of the thorax are expected to improve injury prediction capabilities. While the contribution of the bony structure is well quite well understood in injury biomechanics, the role of the soft tissue such as the ICM in the chest deformation has yet to be quantified.

The ICM are located in the intercostal space and help to expand and shrink the size of the chest cavity during breathing. They are made of three layers named external, internal and innermost layers or intercostal muscles. The internal ICM, located inside the ribcage, extend from the front of the ribs and go around back, past the bend in the ribs. The external ICM, located outside the ribcage, wrap around from the back of the rib almost to the end of the bony part of the rib in front. The fibers in the external and internal layers are orientated diagonally with respect to the ribs, and run in opposite directions. ICM demonstrate a number of complex features including nonlinearity, incompressibility, viscoelasticity and anisotropy that are not yet well described [12].

Global Human Body Models Consortium, GHBMC, a project that try to maintain and make available Human Body Models on a wide scale basis for purposes of improving human safety by allowing mathematical assessments of possible real world injury conditions. Mathematical Human Body Modeling analysis can enable assessment of more real world injury scenarios to allow for engineering improvements to help prevent potential human injury.

Trying to use this promising project (GHBMC) in modelling the side impact of Leport et al [13], we found that this project is missing to include a realistic constitutive modelling of the ICM. The available model in this project is a simplified model that allow to put only an approximate modulus of elasticity, however, trying to use this project by using different values of elasticity modules gave different estimates of the number and location of fractured ribs, Figure 1. The conclusion is that intercostal muscles are very important in the FE modelling of the thorax.

The objective of this paper was to introduce an experimental and theoretical analysis to quantify the effect of the fiber orientation on the mechanical response of the ICM. Tensile tests were performed on ICM samples harvested on one post-mortem human subject, and an optical system was used to measure the strain field on the external layer. Next, a theoretical framework was outlined to develop a constitutive model of the ICM based on an optimization scheme for determining the material parameters.

2. **EXPERIMENTAL WORK**

Three specimens of intercostal muscles were extracted from one post-mortem human subject (70 year old, 160 cm tall, 60 kg): one sample (#A) located between ribs 8 and 9 from the anterior aspect of the rib cage, and two samples (#B and #C) located between ribs 9 and 10 in the lateral and posterior aspects of the rib cage (Figure 2). The dimensions of the ICM specimens are detailed in Table 1. Each sample consisted of rectangles of ICM connected to the adjacent superior and inferior sections of rib, and included the entire depth of the muscle wall and the soft tissue (parietal pleura) attached to the internal surface of the ICM (Figure 2). Prior to their excision, the two rib sections were connected to a wire of copper that maintained their relative position. Once harvested, the angle of the muscle fibers with respect to the inferior rib was measured for the internal and external layers, and the rib sections were potted in blocks (approx. 50 mm × 50 mm × 25 mm deep) of Fast Cast® casting resin (Goldenwest Manufacturing, Inc.).

Prior to testing, each of the specimens was soaked in body temperature (37° C) saline solution for about 2 hours, to allow them to rehydrate if needed. This soaking step was shown to be effective to maintain the tissue in good condition [11], as the tests were performed in open air at room temperature. After this soaking time, each specimen was removed from the soaking solution and the surface was patted dry. The anterior surface of the specimen (i.e. the ICM outer layer) was then covered with a black and white speckle pattern. An optical system was used to measure the strain during the experiment: the deformation of the painted surface was recorded with two high-speed cameras (NAC-GX1) at 2,000 frames per second, with a resolution of 1280×1024 pixels. Prior to recording the images, the two cameras were affixed to a rigid bar, and their orientation was adjusted so that (1) the center of the field of view of each camera was confounded in the focus plane and (2) the angle between the cameras was around 20 degrees (Fig. 3). The Two-camera system was then calibrated so that the surface displacement and strain fields could be calculated with the ARAMIS software package (version 6.2.0, GOM-Optical Measuring Techniques, Germany).

The block containing the inferior rib (inferior block) was connected to a 6-axis load cell, while the superior block was connected to the extremity of the piston of an Instron material tests machine (Model 8874). Once the sample was in position, the copper wire was cut. Each specimen was subjected to a series of three tensile tests. First, each specimen was subjected to a pre-conditioning test imposing a 1 Hz, cyclical (sinusoidal) displacement in tension (no compression) for 20 cycles. The magnitude of the displacement was 5% of the initial length of the muscle. Afterwards, the test machine was reset to the initial (pre-test) specimen position. Then, each specimen was subjected to a tensile dynamic ramp-hold test. A displacement was applied via a 300 mm/s ramp. The magnitude of the displacement was 25% of the initial length of the specimen. After the ramp this position was held for 60 s to observe force relaxation in the specimens. Afterwards, the test machine was again reset to the initial (pre-test) specimen position. Finally, each specimen was subjected to a tensile quasi-static failure test, where a 3 mm/s displacement was applied past the point of failure of the specimen. The applied displacement and the load were recorded with a Dewetron (DEWE-2010 Series, Dewetron, Graz) data acquisition system. For the quasi-static failure tests data were collected at a rate of 10 kHz.

The entire test matrix was provided for completeness, however only the results of the quasi-static failure tests were used in the current study.

3. CONSTITUTIVE MODELING

The intercostal muscles under consideration is assumed to be an anisotropic hyperelastic and continuous solid, which is described by the coordinate system $\mathbf{X}$ in undeformed state. After deformation the solid is described by the coordinate system $\mathbf{x}$. The deformation gradient, $\mathbf{F}$, is defined as $\mathbf{F} = \partial\mathbf{x}/\partial\mathbf{X}$, and the volume ratio, J, as $J = |\mathbf{F}| > 0$.

The deformation gradient can be decomposed into volumetric and distortional deformation, $\mathbf{F} = (J^{1/3})\bar{\mathbf{F}}$. Similarly, for the right Cauchy-Green tensor can be defined as:

$$\mathbf{C} = \mathbf{F}^{\mathrm{T}}\mathbf{F} = (J^{2/3})\bar{\mathbf{C}}, \qquad \bar{\mathbf{C}} = \bar{\mathbf{F}}^{\mathrm{T}}\bar{\mathbf{F}} \tag{1}$$

The Helmholtz free energy, W, is decoupled into the volumetric and isochoric parts. Furthermore, the isochoric part can be divided into an isotropic (independent of fiber orientations) and an anisotropic part:

$$W = W_{\mathrm{vol}}(J) + W_{\mathrm{iso}}(\bar{\mathbf{C}}) + W_{\mathrm{aniso}}(\bar{\mathbf{C}}, \mathbf{a}\otimes\mathbf{a}, \mathbf{g}\otimes\mathbf{g}) \tag{2}$$

where $\mathbf{a}$ and $\mathbf{g}$ are two fiber directions in the undeformed configuration (Fig. 4) that characterizes the anisotropic behavior of the material, with $|\mathbf{a}| = 1$, and $|\mathbf{g}| = 1$.

The isochoric part (isotropic and anisotropic parts) of the strain energy functions can be written in terms of strain invariants and pseudo-invariants: the isotropic part can be written in terms of the strain invariant $\bar{I}_1$ and $\bar{I}_2$, while the anisotropic part can be written in terms of pseudo-invariants, which for two families of fibers are $\bar{I}_4, \bar{I}_5, \bar{I}_6, \bar{I}_7,$ and $\bar{I}_8$ [14]. In the current study, we use only $\bar{I}_4$ and $\bar{I}_6$, since they are the squares of the stretches in the directions of the fibers, and therefore have a physical interpretation [15]. The strain energy in terms of the modified invariants is:

$$W = W_{vol}(J) + W_{iso}(\bar{I}_1, \bar{I}_2) + W_{aniso}(\bar{I}_4, \bar{I}_6) \tag{3}$$

where $\bar{I}_1 = tr\,\bar{\mathbf{C}}$, $\bar{I}_2 = \frac{1}{2}((tr\,\bar{\mathbf{C}})^2 - tr\,\bar{\mathbf{C}}^2)$, $\bar{I}_4 = \mathbf{a}\cdot\bar{\mathbf{C}}\mathbf{a}$, and $\bar{I}_6 = \mathbf{g}\cdot\bar{\mathbf{C}}\mathbf{g}$.

The volumetric part of the strain energy function is given by

$$W_v(J) = \frac{1}{d}(J - 1)^2 \tag{4}$$

The isotropic part of the strain energy function used in this work as a polynomial form, expressed as:

$$W_{iso}(\bar{I}_1, \bar{I}_2) = \sum_{i=1}^{3} a_i(\bar{I}_1 - 3)^i + \sum_{j=1}^{3} b_j(\bar{I}_2 - 3)^j \tag{5}$$

while the anisotropic part of the strain energy function, that is to say the energy function in the fibers, is assumed in the form of an exponential form:

$$W_{aniso}(\bar{I}_4, \bar{I}_6) = \frac{c_1}{2c_2}[\exp(c_2(\bar{I}_4 - 1)^2 - 1)] + \frac{e_1}{2e_2}[\exp(e_2(\bar{I}_6 - 1)^2 - 1)] \qquad (6)$$

In order to determine the constitutive equations for anisotropic hyperelastic materials in term of strain invariants, the strain energy function, W, is differentiated with respect to the tensor $\mathbf{C}$. By means of the chain rule, the second Piola-Kirchhoff (2nd PK) stress, S, can be decomposed into the volumetric and the deviatoric stresses:

$$S = S_{vol} + S_{iso} + S_{aniso} = S_{vol} + S_{dev} \qquad (7)$$

where S_{vol} and S_{dev} are the volumetric and the deviatoric stresses, respectively, which in turn can be expressed as:

$$S_{vol} = p J \mathbf{C}^{-1}, \qquad (8)$$

$$S_{dev} = J^{-2/3}\left(\tilde{S} - \frac{1}{3}(\bar{\mathbf{C}}:\tilde{S})\bar{\mathbf{C}}^{-1}\right) \qquad (9)$$

and,

$$\tilde{S} = 2\frac{\partial W_{dev}}{\partial \bar{\mathbf{C}}} = 2\sum_{\alpha=1,2,4,6}^{4}\frac{\partial W_{dev}}{\partial \bar{I}_\alpha}\frac{\partial \bar{I}_\alpha}{\partial \bar{\mathbf{C}}} \qquad (10)$$

The derivatives of the modified invariants with respect to the deviatoric part of the right Cauchy-Green tensor are written as:

$$\frac{\partial \bar{I}_1}{\partial \bar{\mathbf{C}}} = \mathbf{I}, \; \frac{\partial \bar{I}_2}{\partial \bar{\mathbf{C}}} = \bar{I}_1\mathbf{I} - \bar{\mathbf{C}}, \; \frac{\partial \bar{I}_4}{\partial \bar{\mathbf{C}}} = \mathbf{a}\otimes\mathbf{a}, \; \text{and} \; \frac{\partial \bar{I}_6}{\partial \bar{\mathbf{C}}} = \mathbf{g}\otimes\mathbf{g} \qquad (11a)$$

and the derivatives of the deviatoric part of the strain energy function with respect to the modified strain invariants are:

$$\begin{aligned}
\frac{\partial W_{dev}}{\partial \bar{I}_1} &= a_1 + 2a_2(\bar{I}_1 - 3) + 3a_3(\bar{I}_1 - 3)^2 \\
\frac{\partial W_{dev}}{\partial \bar{I}_2} &= b_1 + 2b_2(\bar{I}_2 - 3) + 3b_3(\bar{I}_2 - 3)^2 \\
\frac{\partial W_{dev}}{\partial \bar{I}_4} &= c_1(\bar{I}_4 - 1)\exp(c_2(\bar{I}_4 - 1)^2) \\
\frac{\partial W_{dev}}{\partial \bar{I}_6} &= e_1(\bar{I}_6 - 1)\exp(e_2(\bar{I}_6 - 1)^2)
\end{aligned} \qquad (11b)$$

The Cauchy (true) stress can be computed from the 2nd PK:

$$\boldsymbol{\sigma} = J^{-1}\mathbf{F}\, S\, \mathbf{F}^T \qquad (12)$$

For uniaxial tension, assuming full incompressibility, i.e., $J=1$, $\lambda_1 = \lambda$ and, $\lambda_2 = \lambda_3 = \lambda^{-1/2}$, the deformation gradient becomes:

$$\mathbf{F} = \begin{bmatrix} \lambda & 0 & 0 \\ 0 & \lambda^{-1/2} & 0 \\ 0 & 0 & \lambda^{-1/2} \end{bmatrix}$$

Defining the fiber orientation vectors as $\mathbf{a} = \{\cos\beta_1, \sin\beta_1, 0\}$ and $\mathbf{g} = \{\cos\beta_2, \sin\beta_2, 0\}$, equations (11a) yields to (for uniaxial tension):

$$\frac{\partial \bar{I}_1}{\partial \bar{\mathbf{C}}} = \mathbf{I}, \qquad \frac{\partial \bar{I}_2}{\partial \bar{\mathbf{C}}} = \begin{bmatrix} 2\lambda^{-1} & 0 & 0 \\ 0 & \lambda^2 + \lambda^{-1} & 0 \\ 0 & 0 & \lambda^2 + \lambda^{-1} \end{bmatrix},$$

$$\frac{\partial \bar{I}_4}{\partial \bar{\mathbf{C}}} = \begin{bmatrix} \cos^2(\beta_1) & \sin(\beta_1)\cos(\beta_1) & 0 \\ \sin(\beta_1)\cos(\beta_1) & \sin^2(\beta_1) & 0 \\ 0 & 0 & 0 \end{bmatrix},$$

$$\text{and } \frac{\partial \bar{I}_6}{\partial \bar{\mathbf{C}}} = \begin{bmatrix} \cos^2(\beta_2) & \sin(\beta_2)\cos(\beta_2) & 0 \\ \sin(\beta_2)\cos(\beta_2) & \sin^2(\beta_2) & 0 \\ 0 & 0 & 0 \end{bmatrix}$$

where β_1 and β_2 are the angles of the external and internal intercostal muscles fibers, respectively, measured counterclockwise from direction 1-axis (Fig. 4).

Combining the above equations with equation (7) yields to:

$$\begin{bmatrix} S_{11} & S_{12} & S_{13} \\ S_{21} & S_{22} & S_{23} \\ S_{31} & S_{32} & S_{33} \end{bmatrix} = p \begin{bmatrix} \lambda^{-2} & 0 & 0 \\ 0 & \lambda & 0 \\ 0 & 0 & \lambda \end{bmatrix} + \begin{bmatrix} \tilde{S}_{11} & \tilde{S}_{12} & \tilde{S}_{13} \\ \tilde{S}_{21} & \tilde{S}_{22} & \tilde{S}_{23} \\ \tilde{S}_{31} & \tilde{S}_{32} & \tilde{S}_{33} \end{bmatrix} - \frac{\lambda^2 \tilde{S}_{11} + \lambda^{-1}(\tilde{S}_{22} + \tilde{S}_{33})}{3} \begin{bmatrix} \lambda^{-2} & 0 & 0 \\ 0 & \lambda & 0 \\ 0 & 0 & \lambda \end{bmatrix}$$

$$(13)$$

Since the stresses along directions 2 and 3 (Figure 4) are zero in the case of the uniaxial test, an expression for the hydrostatic pressure can be obtained from equation (13). Then substituting the expression obtained for the hydrostatic pressure for the stress S_{11} in 1-axis yields to the following constitutive relation:

$$S_{11} = \tilde{S}_{11} - \frac{\tilde{S}_{33}}{\lambda^3} \tag{14}$$

where;

$$\tilde{S}_{11} = 2[a_1 + 2a_2(\bar{I}_1 - 3) + 3a_3(\bar{I}_1 - 3)^2] + 2[b_1 + 2b_2(\bar{I}_2 - 3) + 3b_3(\bar{I}_2 - 3)^2](2\lambda^{-1})$$
$$+ 2[c_1(\bar{I}_4 - 1)\exp(c_2(\bar{I}_4 - 1)^2)]\cos^2(\beta_1)$$
$$+ 2[e_1(\bar{I}_6 - 1)\exp(e_2(\bar{I}_6 - 1)^2)]\cos^2(\beta_2)$$

$$\tilde{S}_{33} = 2[a_1 + 2a_2(\bar{I}_1 - 3) + 3a_3(\bar{I}_1 - 3)^2] + 2[b_1 + 2b_2(\bar{I}_2 - 3) + 3b_3(\bar{I}_2 - 3)^2](\lambda^2 + \lambda^{-1})$$

The material parameters a_1, a_2, a_3, b_1, b_2, and b_3 are related to the isotropic part of the muscles response (the matrix), while c_1, c_2, e_1, and e_2 are related to the anisotropic part (the fibers) of the response. All these parameters were estimated through an optimization process and an inverse FE approach.

4. VISCOELASTIC MODELING

The viscoelastic behaviour of the ICM is modeled via the relaxation function using a Prony series. Values of the shear and bulk modulus would be enough as the starting values of the

material properties over the time, which are representative of deviatoric and volumetric parts of the stress, respectively, as expressed in the following equations [14]:

$$\sigma = \sigma_{deviatoric} + \sigma_{volumetric} , \qquad (15)$$

$$\sigma = \int_0^t 2G(t-\tau)\frac{de}{d\tau}d\tau + I\int_0^t K(t-\tau)\frac{d\Delta}{d\tau}d\tau , \qquad (16)$$

where σ is Cauchy stress, e and Δ are deviatoric parts of the strains, $G(t)$ and $K(t)$ are shear and bulk modulus functions, respectively, t and τ are current and past time, respectively, and I is identity matrix.

Relating to the shear and bulk modulus over the time, Prony series can be proposed by the flowing formulas [14]:

$$G = G_0\left[\alpha_\infty^G + \sum_{i=1}^{n_G} \alpha_i^G \, exp\left(-\frac{t}{\tau_i^G}\right)\right] \qquad (17)$$

$$K = K_0\left[\alpha_\infty^K + \sum_{i=1}^{n_K} \alpha_i^K \, exp\left(-\frac{t}{\tau_i^K}\right)\right] \qquad (18)$$

where superscript shows belonging to shear or bulk modulus, and subscript indices the number of series component, $\alpha_i = \frac{G_i}{G_0}$ and τ_i are relaxation time constants for each Prony series component. α_i that can be calculated at t equal to zero will be obtained from equation (17) as,

$$1 = \alpha_\infty + \sum_{i=1}^n \alpha_i,$$

it means that $\alpha_\infty = 1 - \sum_{i=1}^n \alpha_i$, so equation (17) can be written as :

$$G_0 = G_0\left[\alpha_\infty^G + \sum_{i=1}^{n_G} \alpha_i^G\right] \qquad (19)$$

There are only two constants α_i and τ_i which should be determined by a relaxation test. In the series, the initial values of G and K would be taken into account at time equal to zero. For finding the coefficient of the bulk function, the same above procedure will be followed.

5. ARAMIS

ARAMIS is a non-contact optical 3D deformation measuring system. ARAMIS analyzes, calculates and documents deformations. The graphical representation of the measuring results provides an optimum understanding of the behavior of the measuring object. ARAMIS recognizes the surface structure of the measuring object in digital camera images and allocates coordinates to the image pixels. The first image in the measuring project represents the undeformed state of the object, Figure 5*a*.

After or during the deformation of the measuring object, further images are recorded. Then, ARAMIS compares the digital images and calculates the displacement and deformation of the object characteristics.

If the measuring object has only a few object characteristics, like it is the case with homogeneous surfaces, you need to prepare such surfaces by means of suitable methods, for example apply a stochastic color spray pattern. In the present work the outer layer surface of the intercostal muscles specimen was covered with a black and white speckle pattern. The deformation of the

painted surface was recorded with two high-speed cameras (NAC-GX1) at 2,000 frames per second, with a resolution of 1280×1024 pixels.

ARAMIS observes the deformation of the specimen through the images by means of various square or rectangular facets. Then, the *Deformation Gradient Tensor*, **F**, is calculated from tracking these images. Subsequently, the strain values or vector can be calculated.

6. RESULTS

6.1 Tensile Tests

The stress and stretch were obtained from the force and displacement: the stress was defined as the force to initial average cross section ratio, and the stretch as the displacement to initial average length ratio using the dimensions of the samples presented in Table 1. For the three samples (Figure 6), a toe region was observed, followed by quasi-linear response after about 20 % of stretch.

The ramp-hold tests (or relaxation test) is shown in Fgiure 7 for Sample A, the data are processed and filtered with MATLAB. It is seen from the figure that there is an initial overshoot, after that the muscles relaxed quickly at the first few seconds, then, the relaxation rate slow down to reach a flat situation.

6.2 Fiber Orientation

The angles of the internal and external fibers for all specimens were measured experimentally, Table 2, the measurements was from the lower ribs in counter-clockwise direction.

6.3 Determination of Material Parameters

Material parameters were adjusted using the Matlab ™ Optimization Toolbox version 7.11 (The MathWorks Inc.). Based on the information of the fiber orientation presented in Table 2, a fitting of the experimental data from the uniaxial tests was implemented using the Levenberg–Marquardt algorithm to solve the nonlinear curve fitting in the least squares sense. The materials parameters obtained from the optimization process with 95% confidence bounds for the three tested ICM samples are summarized in Table 3.

7. FINITE ELEMENT MODELING

After calculating the material parameters using the Matlab ™ Optimization Toolbox, the FE analysis was conducted using the ANSYS APDL software package (ANSYS, Inc.). The problem was solved as a 3-D solid, meshed with high order 3-D 20-node solid element with quadratic displacement interpolation (SOLID186 in ANSYS). The NLGEOM command, for nonlinear geometry solution option, was also enabled. Finally, the APDL command TB-AHYPER was invoked: this command enables the modeling of anisotropic hyperelastic materials based on the definition of a potential-based-function with parameters that define the volumetric part and the isochoric part (the matrix and the fiber directions). Once the mesh was created, the hyperelastic parameters were initialized based on the results obtained from MATLAB.

In order to demonstrate the effect of the fiber orientation on the ICM response, i.e. the anisotropic behavior of the muscles, the problem was first solved for Sample A as an isotropic hyperelastic one, assuming *no fibrous structure*. It was observed that the strain pattern was approximately symmetrical (Fig. 8a). When anisotropy was assumed (Fig. 8b), using fiber angles of 55° for the internal layer and 145° for the external layer, the strain field was found to be

unsymmetrical (Fig. 8b) . This demonstrates that there is a significant difference in muscles response between the two assumptions. The same conclusion was drawn for Samples B & C.

8. DISCUSSION

8.1 Experimental Results

The ICM exhibited a common soft tissue behavior with a toe region up to approximately 20 % where little stress is generated. Samples B and C exhibited non-linearity for 1.42 and 1.57 of stretch ratios. The reasons behind these sudden drops (Sample B-Figure 6) of the stress are unclear. Two assumptions can be made. First, this could be an experimental artifact: the strain analysis relies on a speckle pattern that was created with an oil-based paint that hardens when it dries, and the drop in the stress could have been caused when the paint cracked. Indeed, because of the large deformation sustained by the ICM sample, the paint cracked in several areas, when the deformation of the ICM reached the paint failure threshold. The choice of paint was a trade-off between its compliance and its ability to properly adhere to a humid surface. The second assumption is that damage occurred because of fiber decohesion or fracture. The modeling approach in the present study did not account for the damage or fracture, as this would have required to unload and load the sample several times identify the parameters for a damage evolution law. As only three samples were tested, it is not possible to draw extensive conclusions regarding the location dependence of the ICM mechanical properties. However, it would make sense for the ICM to have location dependent properties because the mass of the thorax is not equally distributed within the ribcage.

8.2 Fiber Orientation

The assumption of isotropy may predict the stiffness and response for the muscles when subjected to the same boundary condition as that during experiments, it was shown that anisotropic modeling, i.e. including the contribution of the fibers, resulted in a more accurate estimate of the strain. Indeed, the strain fields in the external layer of the ICM were significantly different under these two assumptions. Therefore, assuming an isotropy behavior prevents from accurately predicting the values and locations of the maximum stress during an impact, and consequently the simulation results could lead to the incorrect prediction of the number and location of the rib fractures, to ultimately yield to a wrong estimation of the risk incurred by a belted vehicle occupant during an impact.

8.3 Material Parameters

The ICM were assumed to behave as a hyperelastic anisotropic and incompressible soft tissue. They were assumed to be consisted of two families of fibers that were assumed to be straight. The response of the anisotropic part of the strain energy and the resulted constitutive relation was assumed to related to the fibers only, while the isotropic part was related to an effective matrix which includes the response of the innermost layer. At low strain, the isotropic part of the muscles (the matrix material) is the effective response, and as the strain increases the stiffening of the ICM muscle occurs and the fiber response becomes the dominant response (the matrix material is significantly less stiff than the fibers). The response of the ICM was found to be location dependent, as even neighboring samples (Samples B & C) give different responses (Figure 6). Six material parameters (a_1, a_2, a_3, b_1, b_2, and b_3) were used to describe the matrix material depending on the polynomial form of strain energy, while an exponential form of the strain   energy   function   with   two   material   parameters   was   used   for   each   layer

(c_1, c_2, for one layer, and e_1, e_2 for the other). All these parameters were estimated through an optimization process using MATLAB. The material parameters c_1 and c_2 were assumed to have the same numerical values as e_1 and e_2, respectively, and these parameters were constrained to be greater than zero to have some physical meaning (the fibers are assumed active only in extension). The fitting procedure developed in this study demonstrates the predictive ability of the current approach to estimate the anisotropic stiffening due to fiber reinforcement at large strains.

9. <u>CONCLUSIONS</u>

A constitutive model and an inverse FE analysis were developed to determine the anisotropic material properties of ICM. In addition to matching the stress-strain relationship, the optimization scheme constrained the computational model to match the experimental strain measured in several locations of the ICM external layer and compared with that obtained from the optical strain measurement system (ARAMIS). The optimized model was then used to evaluate the effects of the anisotropic behavior of the muscles, i.e. the effect of fibers in each layer, on the predicted mechanical behavior. The fibers orientations for the three samples was found to vary from 145° to 155° for the external layers, and from 55° to 70° for the internal layers (the angles were measured locally from the lower rib in counter-clockwise direction). The fitting procedure demonstrated the ability of the proposed model to account for the anisotropic stiffening due to fibers reinforcement at large strains. It was shown that localization in the strain field was predicted by the computational model only when the ICM was modeled as anisotropic.

The results of the parameters optimization revealed that the ICM exhibited a high degree of anisotropy. While including fiber orientation of the ICM in a FE model of the thorax adds extra complexity to the model, the present study demonstrates that it may be a necessary step to properly match the effective stiffness of the ICM. Indeed, it is anticipated that a more accurate material model for the ICM will contribute to a better prediction of the complex strain field in the rib cage that will ultimately lead to a better understanding of the injury mechanisms.

<u>References</u>

[1] Lizee E, Robin S, Song E, Bertholon N, Lecoz JY, Besnault B, Lavaste F, Development of a 3D finite element model of the human body, *Proc. 42nd Stapp Car Crash Conference*, pp. 115-138, *Society of Automotive Engineers*, Warrendale, PA, 1998.

[2] Deng YC, Kong W, Ho H, "Development of a finite element human thorax model for impact injury studies", *Society of Automotive Engineers,* 1999-01-0715, Warrendale, PA, 1999.

[3] Robin S, HUMOS: Human model for safety—a joint effort towards the development of refined human-like car occupant models, *Proc. 17th Enhanced Safety of Vehicles Conference*, Paper 297, 2001.

[4] Shah CS, Yang KH, Hardy WN, Wang K, King AI, Development of a computer model to predict aortic rupture due to impact loading. *Stapp Car Crash Journal*, 45:161-182, 2001.

[5] Kimpara H, Lee J, Yang K, King A, Iwamoto M, Watanabe I, Miki K, Development of a three-dimensional finite element chest model for the 5th percentile female, *Stapp Car Crash Journal*, 49:251-269, 2005.

[6] Zhao J, Narwani G, Development of a human body finite element model for restraint system R & D application, *Proc. 19th International Technical Conference on Experimental Safety of Vehicles*, 2005.

[7] Duprey S, Bruyere K, Verriest J-P, Influence of geometrical personalization on the simulation of clavicle fractures, *J. Biomechanics*, 41:200-207, 2008.

[8] Charpail E, Trosseille X, Petit P, Laporte S, Lavaste F, Vallancien G, Characterization of PHMS ribs: a new test methodology, *Stapp Car Crash Journal,* 49:1-16, 2005.

[9] Kindig M, Lau A, Kent R, Biomechanical response of ribs under quasistatic frontal loading, *Traffic Injury Prevention,* 12(4):377-387, 2011.

[10] Lau A, Oyen ML, Kent RW, Murakami D, Torigaki, T, Indentation stiffness of aging human costal cartilage, *Acta Biomaterialia*, 4:97-103, 2008.

[11] Forman J, del Pozo de Dios E, Arregui Dalmases C, Kent R, The contribution of the perichondrium to the structural mechanical behavior of the costal-cartilage, *J. Biomech. Engineering*, 132(9):094501, 2010.

[12] Hamzah M, Subit D, Boruah S, Forman J, Crandall J, Ito D, Ejima S, Kamiji K, and Yasuki T, "An Inverse Finite Element Approach for Estimating the Fiber Orientations in Intercostal Muscles" *IRCOBI Conference 2013*, IRC-13-88, Sweden.

[13] Leport T, Baudrit P, Potier P, Trosseille X, Lecuyer E, Vallan Cien G, "Study of Rib Fracture Mechanisms Based on the Rib Strain Profiles in Side and Forward Oblique Impact", *55th Stapp Car Crash Conference*, 2011.

[14] Holzapfel GA, Nonlinear Solid Mechanics: A continuum Approach for Engineering, *John Wiley & Sons*, 2000, England.

[15] Holzapfel GA and Gasser TC, A new constitutive framework for arterial wall mechanics and a comparative study of material models, *Journal of Elasticity,* 61:1-48, 2000.

Table 1: Dimensions of the ICM specimens

Sample	Total length (mm)			Muscle length (mm)		Width (mm)		Thickness (mm)	
	Ant	Mid	Post	Ant	Post	Sup	Inf	Ant	Post
A	40.0	41.6	43.4	17.1	16.3	30.0	28.0	4.3	4.7
B	50.0	52.5	53.1	21.2	19.0	28.9	28.3	2.8	2.3
C	52.2	51.6	49.3	18.1	15.3	29.0	29.0	2.5	4.4

Table 2: ICM fiber angles for internal and external layers, measured from the lower ribs.

Sample #	Angle of External layer	Angle of Internal layer
A	145°	55°
B	147°	61°
C	155°	69°

Table 3: Materials parameters obtained from the optimization process for the ICM samples

Sample	Material Parameters for the ICM Samples								
	a_1	a_2	a_3	b_1	b_2	b_3	c_1 & e_1	c_2 & e_2	R^2
A	0.02001	0.01980	3.0e-14	-0.0881	0.0199	-0.1167	0.3100	0.1901	0.978
B	1.42e-6	0.02000	8.2e-14	2.3e-11	0.0198	2.2e-14	0.2885	0.1999	0.981
C	-0.0999	1.92e-6	0.1395	0.01297	6.0e-13	0.08071	0.2913	0.2002	0.995
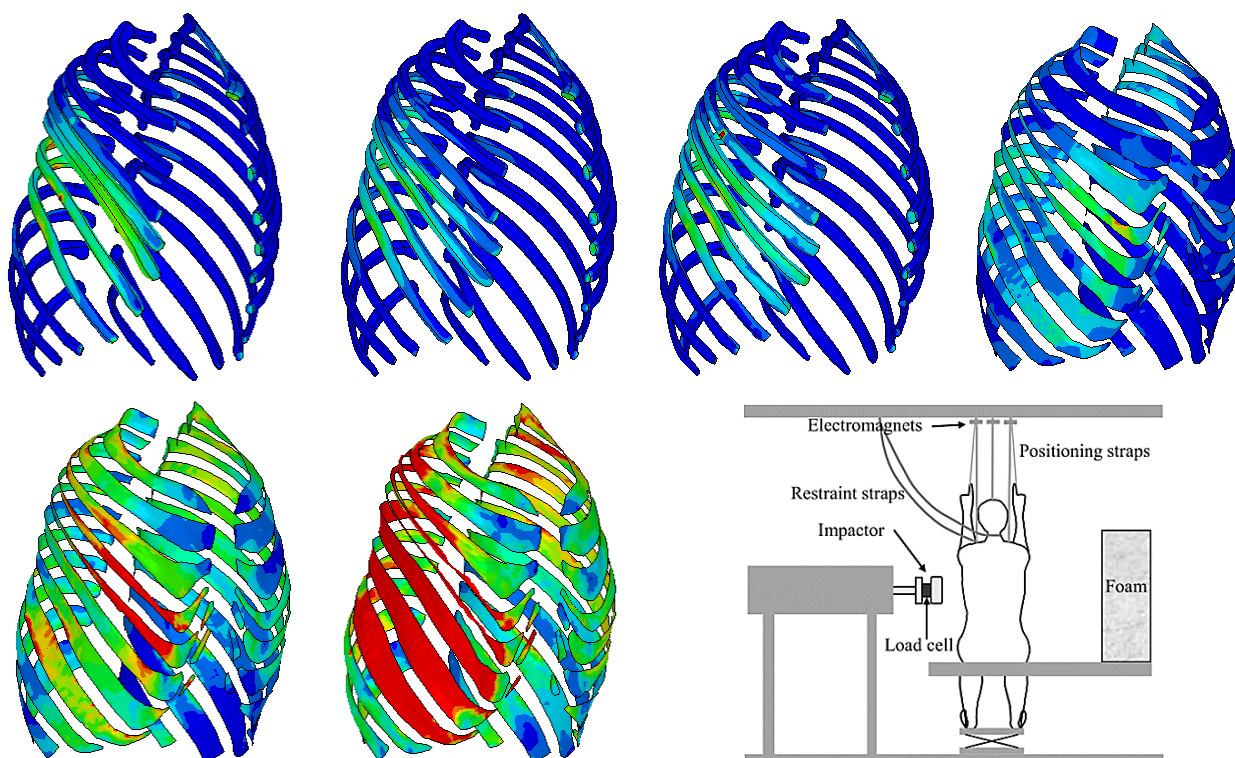
Figure 1. Response of thorax using different values of elasticity modulus of ICM by GHBMC.
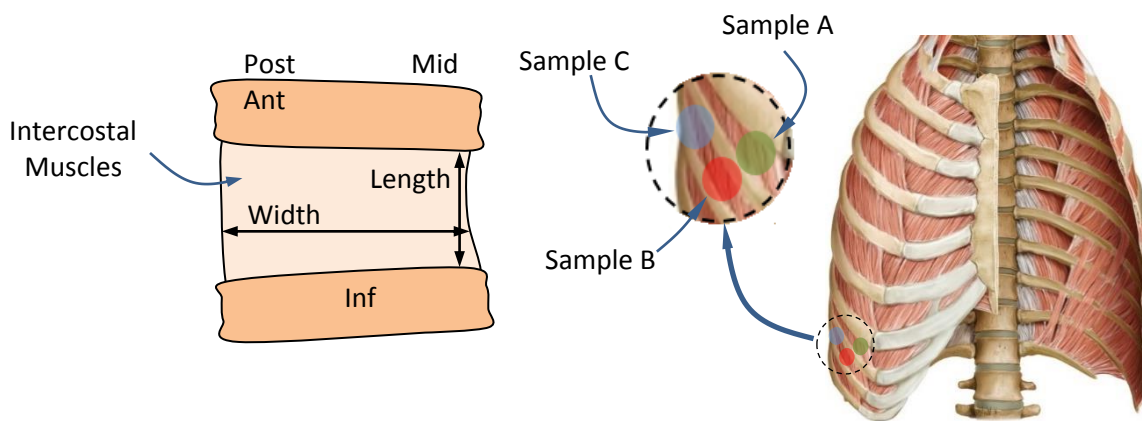
Figure 2. Dimensions and locations of the ICM samples.

Figure 3. Experimental testing and Cameras set-up with lights.
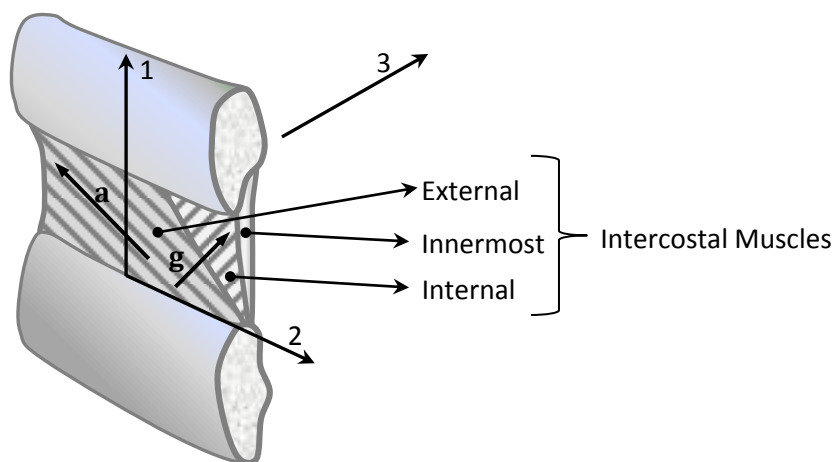
Figure 4. Intercostal muscles layers fibers orientations

(a) speckle pattern   (b) image at 10 % strain   (c) image at 20 % strain
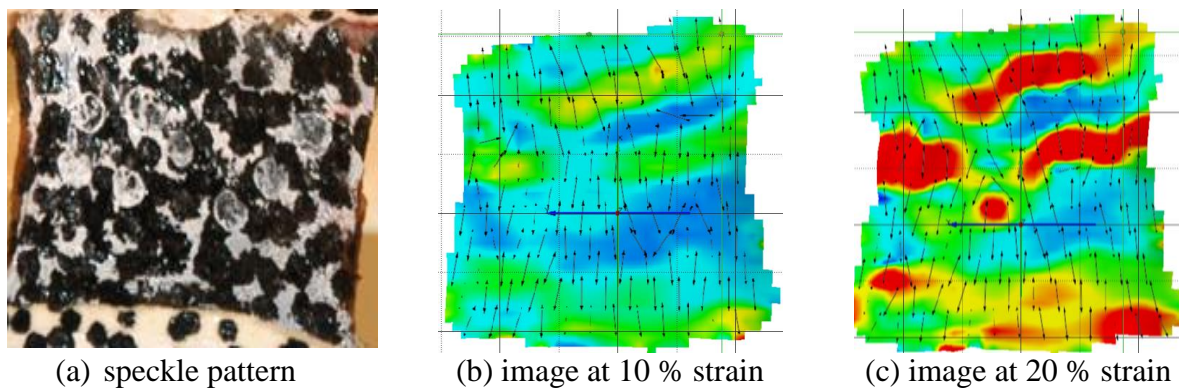
Figure 5. ARAMIS speckle pattern and images correlation.
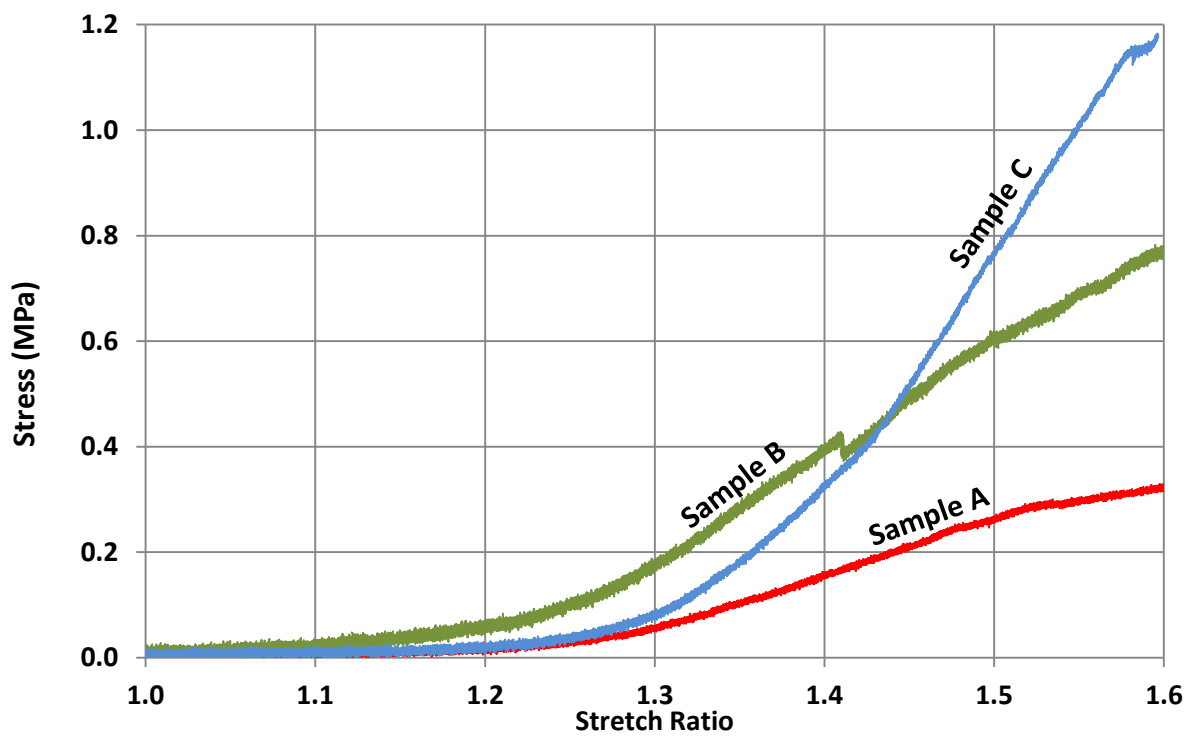
Figure 6. Stress vs. stretch ratio for quasi-static tensile tests.
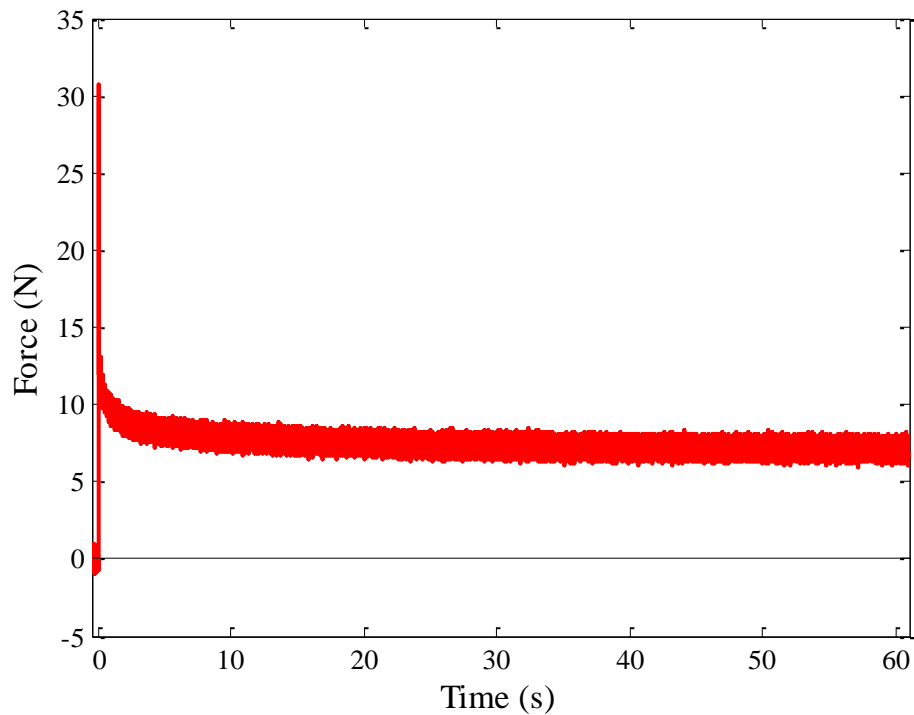
Figure 7. Ramp and test (relation test) for Sample A.
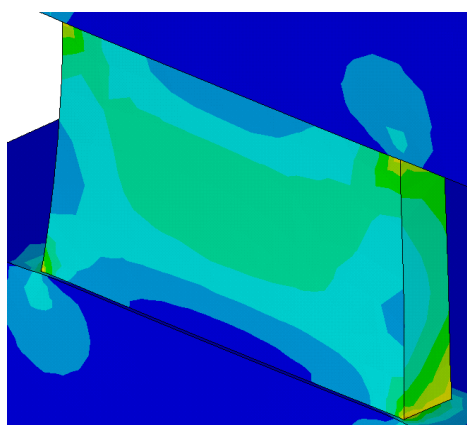
(a)
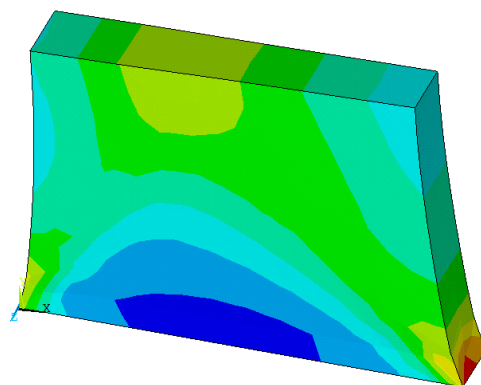
(b)

Figure 7. Effect of fiber orientations on the strain pattern in the ICM for Sample A, (a) Isotropic assumption (no fibers effect), (b) Anisotropic assumption (with fibers effect)